

# A coherently stimulated Brillouin spectrometer

Joel N. Johnson,<sup>1,2,\*</sup> Co Authors,<sup>3</sup> and Ryan O. Behunin<sup>1,2,†</sup>

<sup>1</sup>*Department of Applied Physics and Materials Science,  
Northern Arizona University, Flagstaff, AZ, 86011, USA*

<sup>2</sup>*Center for Materials Interfaces in Research and Applications,  
Northern Arizona University, Flagstaff, AZ, 86011, USA*

<sup>3</sup>*Department, Address*

(Dated: January 28, 2025)

We present a novel coherently stimulated Brillouin spectrometer utilizing a detuned pump-probe design that exploits a relaxation of phase-matching requirements at small lengths, enabling room-temperature traveling-wave phonon spectroscopy at the micrometer scale with sub-10 fW sensitivity. This approach overcomes the limitations of traditional stimulated Brillouin techniques, particularly regarding phase-matching constraints and spatial resolution. We validated our instrument’s sensitivity with 1 cm of UHNA3 fiber and 100  $\mu\text{m}$  of bulk carbon disulfide liquid, demonstrating its capability to measure Brillouin scattering in materials with low Brillouin gain or, with particular advantage, small effective lengths. This advancement opens new possibilities for nanometer-scale Brillouin spectroscopy and the development of nano-acousto-optic devices.

## I. INTRODUCTION

Brillouin scattering, the inelastic interaction between light and acoustic phonons, is a fundamental phenomenon for probing the mechanical and structural properties of materials at microscopic scales. In spontaneous Brillouin scattering, thermally excited acoustic phonons scatter incident light, causing frequency shifts that reveal information about the material’s elastic properties and acoustic modes [1]. However, the weak signal inherent to spontaneous Brillouin scattering often demands long acquisition times and limits spatial resolution, posing challenges for high-resolution material characterization.

Stimulated Brillouin scattering (SBS) uses intense optical fields to amplify the acoustic wave through a nonlinear optical process. In SBS, a strong pump laser interacts with a counter-propagating Stokes wave in the medium, generating acoustic phonons via electrostriction. As the phonon population grows, it further amplifies the Stokes wave. In turn, that amplified Stokes wave interferes with the pump and reinforces the acoustic field, creating a positive feedback loop that drives exponential amplification. This mechanism enables more efficient excitation and detection of acoustic phonons and underpins numerous applications in optical signal processing, sensing, and high-resolution spectroscopy [2–5].

However, conventional SBS techniques struggle with short samples or materials of inherently low Brillouin gain [6, 7]. Because the Stokes amplitude depends on the product of the Brillouin gain coefficient, pump power, and interaction length, small volumes often yield weak signals unless extremely high optical powers are used. Moreover, while backward SBS sends the scattered wave in the opposite direction of the pump, parasitic reflec-

tions and pump leakage can still obscure the Stokes signal, demanding careful optical isolation and sometimes elaborate filtering. These constraints make it difficult to measure thin films or micro- and nanoscale devices, particularly if high optical intensities risk damaging sensitive samples. As a result, standard SBS approaches are not easily adapted to sub-centimeter lengths or low-gain media, prompting the need for new methods that maintain high sensitivity in short interaction regions.

To overcome these challenges, researchers have explored various approaches [8–10]. Techniques based on optical cavities increase the effective interaction length, but require precise alignment and are sensitive to environmental fluctuations [11]. Forward Brillouin scattering methods, such as those demonstrated by Kittlaus et al. [12], offer relaxed phase-matching conditions but introduce increased modal complexity. Meanwhile, coherent probe beam amplification can boost sensitivity, yet it can introduce additional noise and complexity because phase noise in laser sources can cause significant gain fluctuations [13].

Here, we demonstrate a detuned pump-probe design that relaxes the usual phase-matching constraints at short lengths. This approach offers a new route to measure traveling-wave phonons in sub-centimeter or even micrometer-scale samples at room temperature with unprecedented sensitivity. We demonstrate the capabilities of our instrument by measuring Brillouin scattering in 1 cm of ultrahigh numerical aperture (UHNA3) fiber and 100  $\mu\text{m}$  of bulk carbon disulfide ( $\text{CS}_2$ ) liquid. These measurements highlight the instrument’s ability to characterize materials with low Brillouin gain or small effective lengths.

The development of this coherently stimulated Brillouin spectrometer opens new avenues for nanometer-scale Brillouin spectroscopy and advances the characterization and design of nano-acousto-optic devices. It holds promise for pushing research in material science, photonics, and sensing technologies toward higher spatial

---

\* joel.johnson@nau.edu

† ryan.behunin@nau.edu

resolution and sensitivity, marking a significant step toward practical, room-temperature Brillouin-based spectroscopy and sensing solutions.

## II. THEORETICAL FRAMEWORK

### Coherently stimulated four-wave Brillouin scattering

Traditional SBS, illustrated by the schematic in Fig. 1(a) for the Stokes process, is a three-wave mixing process in which incident pump laser light of frequency  $\omega_{\text{Pump}}$  inelastically scatters from a traveling-wave phonon of frequency  $\Omega$  to produce light that is frequency-shifted by the phonon frequency. In the Stokes process the phonon is retreating from the incident laser light and the scattered light is shifted down in frequency ( $\omega_{\text{Stokes}} = \omega_{\text{Pump}} - \Omega$ ). Spatial overlap of the backscattered light with the incident laser light allows for interference of the two optical fields to produce a frequency at the difference of the two ( $\omega_{\text{Pump}} - \omega_{\text{Stokes}}$ ). Since this difference frequency is exactly equal to the frequency of the acoustic field  $\Omega$ , the beating of the incident pump light with the backscattered Stokes light produces an electrostrictive reinforcement of the acoustic wave. This driving of the acoustic wave in turn increases the scattering rate of the incident pump light, producing a positive feedback process and an exponential increase of the amplitude of the backscattered Stokes wave.

Fig. 1(b) illustrates coherently stimulated four-wave Brillouin scattering for the Stokes process. We introduce a strong, controlled external Stokes wave of frequency  $\omega_{\text{Stokes}}$  that drives electrostrictive reinforcement of the acoustic field in the medium. The backscattered Stokes light is normally collected in an SBS process, but the external Stokes laser overwhelms it. To resolve this, we inject light of a distinct frequency  $\omega_{\text{Probe}}$  from an additional external laser which copropagates with the Pump and backscatters in the medium from the strongly driven acoustic field. This produces backscattered Signal light to be collected ( $\omega_{\text{Signal}} = \omega_{\text{Probe}} - \Omega$ ) which is spectrally distinct from the high-powered Stokes laser light.

To describe this interaction and characterize the performance of the instrument, we derive the coupled-wave equations for the four-wave mixing process in Appendix A. These equations describe the relationship between the optical fields and the acoustic field in the material and result in the following expression for the scattered power of the backscattered signal,

$$P_{\text{Sig}} = \frac{1}{4}(G_B L)^2 P_P P_S P_{Pr} \text{sinc}^2\left(\frac{\Delta k L}{2}\right), \quad (1)$$

where  $P_P$ ,  $P_S$ , and  $P_{Pr}$  are the powers of the pump, Stokes, and probe lasers, respectively.  $G_B$  is the effective Brillouin gain, given by

$$G_B = \frac{g_0}{A_{\text{eff}}} \frac{\left(\frac{\Gamma_B}{2}\right)^2}{(\Omega - \Omega_B)^2 + \left(\frac{\Gamma_B}{2}\right)^2}, \quad (2)$$

with the on-resonance gain factor of the material given by

$$g_0 = \frac{\gamma_e^2 \omega^2}{n v c^3 \rho_0 \Gamma_B}. \quad (3)$$

Here,  $\gamma_e$  is the electrostrictive constant,  $\omega$  is the pump frequency,  $n$  is the refractive index of the material,  $v$  is the sound speed of the material,  $c$  is the speed of light,  $\rho_0$  is the mean density of the material, and  $\Gamma_B$  is the Brillouin linewidth, or phonon dissipation rate, of the material. In Eq. 2,  $\Omega_B$  is the resonant Brillouin frequency of the material,  $A_{\text{eff}}$  is the effective area of the material,  $\Delta k$  is the wavevector mismatch between the optical fields, to be discussed next, and  $L$  is the effective length of the material.

### Phase matching relaxation

In all nonlinear optical processes, efficiency is maximized when phase matching conditions are satisfied. A frequency mismatch (energy unconservation) or a wavevector mismatch (momentum unconservation) each result in drastically reduced efficiency of a given process.[14] This can be seen by Eq. 1, where the wavevector mismatch,  $\Delta k$ , is contained within a  $\text{sinc}^2$  function. This  $\text{sinc}^2$  term thereby defines the phase matching bandwidth of the system, notably scaling with effective interaction length  $L$ .

We apply this wavevector mismatch allowance to the pump and probe waves ( $\Delta k = k_{\text{Pump}} - k_{\text{Probe}}$ ) so that the backscattered signal is different than the applied Stokes wave. This choice allows for selection of the signal and rejection of the Stokes with a bandpass filter. Expressed in terms of wavelengths, this gives

$$\Delta k = \frac{4\pi n \Delta \lambda}{\lambda_{\text{Pump}} \lambda_{\text{Probe}}} \approx \frac{4\pi n \Delta \lambda}{\lambda_{\text{Pump}}^2}. \quad (4)$$

We can apply this to the phasematching bandwidth term to find the fraction of maximum scattered power,  $\Phi$ , that can be expected for a given interaction length,  $L$ , and phase mismatch  $\Delta \lambda$  between the pump and probe,

$$\Phi \equiv \text{sinc}^2\left(\frac{2\pi n \Delta \lambda L}{\lambda_{\text{Pump}}^2}\right). \quad (5)$$

Using this expression for  $\Phi$ , we see that for an effective length of 1 m, a wavelength mismatch of only 0.6 pm from



FIG. 1: Illustration of 4-Wave Brillouin Scattering.

a typical wavelength of  $1.55\,\mu\text{m}$  pump light in UHNA3 fiber drops the scattered power to half of the maximum. However, for shorter effective lengths the wavevector mismatch becomes more forgiving; a  $36\,\text{pm}$  mismatch preserves 82.5% of the maximum signal for a length of  $1\,\text{cm}$  under identical conditions. This separation translates to about  $4.5\,\text{GHz}$ , providing enough spectral separation for the backscattered signal to be isolated from the applied Stokes light.

Furthermore, for decreasing lengths, Eq. 5 predicts an increase in the fraction of maximum signal produced, given equivalent pump-probe detuning, as the  $\text{sinc}^2$  function is sampled closer to its peak center. Alternatively, as length decreases, the probe may be further detuned from the pump and still achieve the same fraction of the maximum signal as for longer lengths, perhaps offering a slight advantage in noise reduction. It should be noted that the scattered power, as given by Eq. 1, scales with the square of the effective length. Thus, while smaller lengths allow for the ability to capture a larger fraction of this maximum scattered power, the actual amount of scattered power decreases dramatically as length decreases.

### III. METHODS

#### Instrument design

Figure 2 shows the instrument's design. A pump and Stokes wave is synthesized from a single tunable laser source for coherent stimulation of a sample. The pump wave ( $\omega_{\text{Pump}}$ ) is amplified by an erbium-doped fiber amplifier (EDFA) and passed through a variable optical attenuator (VOA) for power control. The output is then polarization-controlled to reflect at a polarizing beam splitter (PBS) for injection into the sample. For Stokes synthesis, an AC signal ( $\Omega$ ) is supplied to an intensity modulator (IM) with carrier frequency nulled and a tunable filter is used to select the lower-frequency Stokes side band ( $\omega_{\text{Pump}} - \Omega$ ). This Stokes light is then amplified by an EDFA, passed through a VOA, and polarization-controlled to reflect at a second PBS for counter-propagation to the pump through the sample.

A separate tunable laser is used to supply a probe wave

( $\omega_{\text{Probe}} = \omega_{\text{Pump}} + \Delta k$ ) and local oscillator (LO). Probe light is amplified by an EDFA and passed through a VOA and a polarization controller aligns the polarization for transmission through the first PBS whereby it copropagates with the pump through the sample. Backscattered light exits the sample and transmits back through the first PBS, whereas the orthogonally polarized Stokes light reflects at this same point to be diverted to a tap for power monitoring. The backscattered signal ( $\omega_{\text{Signal}} = \omega_{\text{Probe}} - \Omega$ ) then routes through two subsequent circulators for spectral filtering by a  $5\,\text{GHz}$  bandpass tunable filter. This filter allows the desired backscattered signal to pass while rejecting any reflected probe light as well as any reflected, transmitted, or backscattered light from the pump or Stokes waves that was not already diverted by the PBS.

The filtered signal then heterodynes via a 99-1 splitter with the LO which is frequency-upshifted by an acousto-optic modulator (AOM) ( $\omega_{\text{LO}} = \omega_{\text{Probe}} + \omega_{\text{AOM}}$ ) and controlled to be copolarized with the signal. Of the resulting frequencies from the heterodyne process, only the difference frequency term is considered, as all others are beyond the range of detection. This heterodyned signal ( $\omega_{\text{Signal}} = \Omega + \omega_{\text{AOM}}$ ) is then captured by a photodiode detector and heterodyned again by a radio frequency (RF) mixer with a second AC signal ( $\Omega + \omega_{\text{AOM}} - \omega_{\text{Lock}}$ ), where  $\omega_{\text{Lock}}$  is a fixed-frequency to be detected by a lock-in amplifier set to this frequency after being passed through a low-pass filter and amplified by an RF amplifier. Synchronous sweeping of both AC signals, each involving  $\Omega$ , allows for  $\omega_{\text{Lock}}$  to remain fixed throughout measurement over a frequency range.

#### Experimental Techniques

We optimized the signal-to-noise ratio (SNR) of our instrument through specific design choices and device settings. Our setup simultaneously generates pump, Stokes, and probe optical fields for coherently stimulated Brillouin scattering. The pump laser provides  $\sim 45\,\text{mW}$  total output, of which 10% is split and amplified to  $\sim 0.5\,\text{W}$  for the pump field; the remaining 90% is frequency-shifted and amplified to  $\sim 1\,\text{W}$  for the Stokes field. Likewise, the probe laser also outputs  $\sim 45\,\text{mW}$ , with 10% ampli-

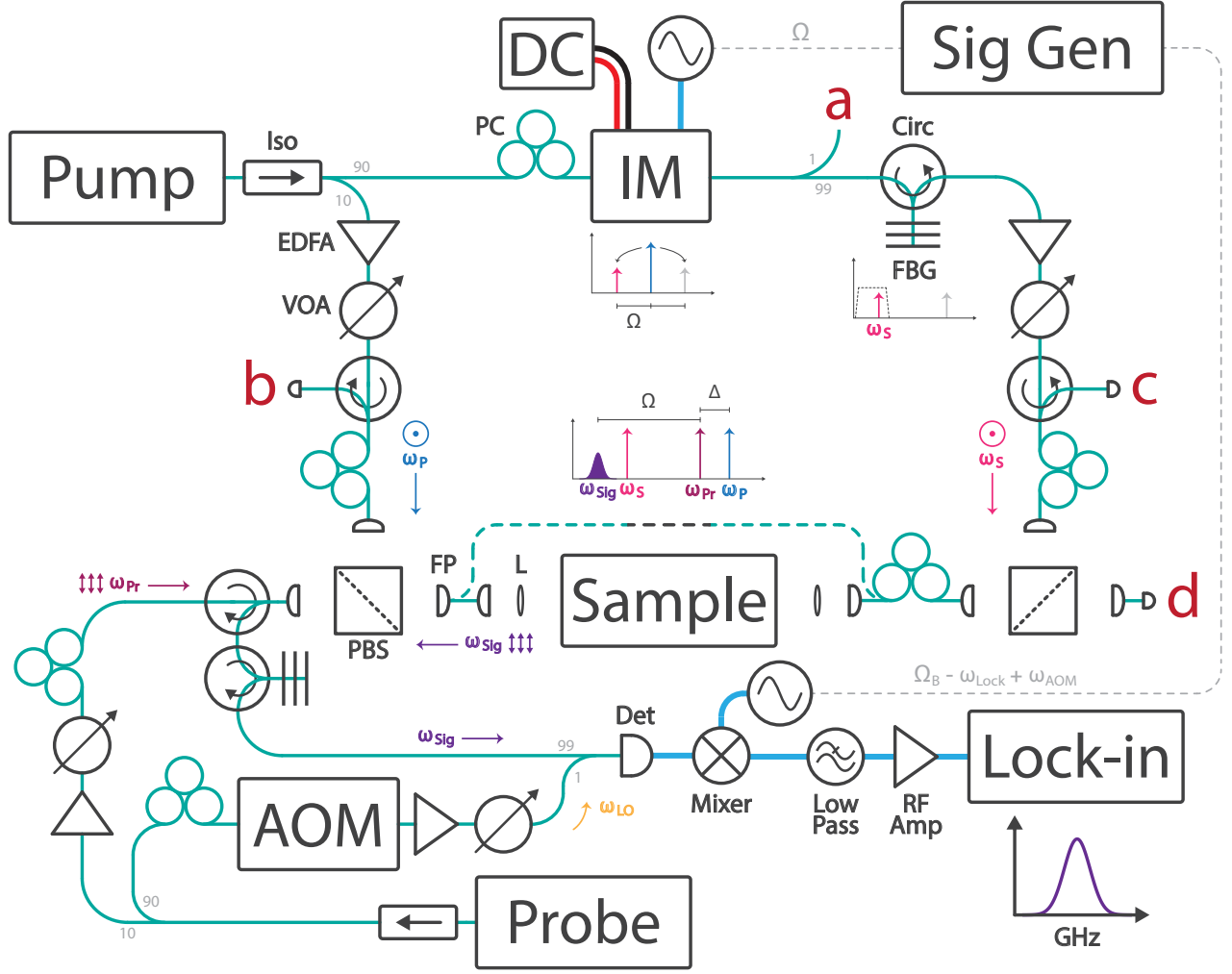


FIG. 2: Design schematic of a coherently stimulated phonon spectrometer. A tunable continuous-wave (CW) laser at approximately 1.55  $\mu\text{m}$  emits light that passes through an isolator (Iso) and a splitter, diverting 10% to a 27 dBm EDFA followed by a variable optical attenuator (VOA). This pump light ( $\omega_P$ ) is polarization-controlled to reflect off a polarizing beam splitter (PBS) and is recoupled to fiber via a fiber port (FP), then directed to the sample either by direct fiber coupling or through a pair of FPs and lenses (L) for free-space samples. After passing through the sample, the pump light traverses a corrective polarization controller that mitigates fiber twists and bends before reflecting off a second PBS, where it is routed to port (c) for power monitoring. To synthesize the Stokes wave, a 90% split from the original pump is processed through an intensity modulator (IM) and a fiber Bragg grating (FBG), generating a Stokes sideband downshifted from the pump by  $\Omega$ . This frequency shift is swept via a signal generator to capture  $\Omega_B$ . A 99/1 splitter provides a tap at port (a) to optimize Stokes synthesis. The Stokes wave ( $\omega_S$ ), amplified by a 1 W EDFA and VOA-controlled, counter-propagates along the pump path and is monitored at port (b). A second tunable CW laser, detuned from the pump, generates the probe wave ( $\omega_{Pr}$ ), which is amplified by a 1 W EDFA, attenuated variably, and polarization-controlled to pass through the initial PBS where it is incident on the sample. Backscattered signal light ( $\omega_{Sig}$ ) transmits back through the PBS, while unscattered probe light transmits to a power meter at port (d). A circulator parts the signal from the probe path, with an FBG filtering out any unwanted noise or Stokes light. Finally, the signal is heterodyned with an EDFA-amplified, AOM-shifted local oscillator (LO) derived from the probe laser and directed to a photodiode for detection. The resulting RF signal is mixed with an AC LO supplied by the signal generator which sweeps synchronously with the Stokes synthesis frequency, and collected by a lock-in amplifier for data processing.

fied to  $\sim 1$  W for the probe field and the remaining 90% reserved for the local oscillator (LO). To combine the backscattered signal and LO with minimal loss, we use a 99/1 splitter instead of a typical 50/50, preserving 99% of the signal. The LO is therefore amplified to  $\sim 230$  mW so the total optical power at the detector remains below the 2.4 mW damage threshold. After detection, the electronic signal is mixed with a 17 dBm AC reference and further amplified by 23 dBm before input to the lock-in amplifier. We find that running both the pump and probe lasers in “whisper” mode (as opposed to “dither”) significantly enhances the measured SNR.

We use a Zurich Instruments HF2LI 50 MHz lock-in amplifier whose demodulator settings are carefully tuned to maximize SNR. A 10 MHz reference clock from the signal generator is fed into the lock-in to synchronize timing. The input-signal range, which sets the analog input amplifier’s gain, should exceed the measured signal (including any DC offset) by at least a factor of two. This is best achieved by using the lock-in software’s *auto* feature, which continuously adjusts the range over a rolling 100 ms window. We set the input coupling to AC, insert a high-pass filter to remove DC components, and choose 1 M $\Omega$  input impedance. For noise suppression, we also engage the lock-in’s eighth-order low-pass filter (roll-off 48 dB Oct $^{-1}$ ) and sample the data at 1.84 MSas $^{-1}$ , the maximum rate available.

Further SNR improvements are gained by narrowing the lock-in’s low-pass filter bandwidth to match both the sub-Hz natural linewidth of the heterodyne signal and the thermally-driven frequency drift of the apparatus. After a  $\sim 30$  min warm-up, we observe less than 100 Hz of drift in the detected signal frequency, so we typically set a 100 Hz low-pass bandwidth for multi-hour measurements. For shorter scans ( $< 15$  min), we can reduce this bandwidth to 40 Hz if needed. In addition to linewidth variability, the signal’s center frequency can shift due to thermal changes in the AOM and related electronics. Although  $\Omega$  is nominally controlled to sub-hertz precision by the signal generator, our AOM’s shift  $\omega_{\text{AOM}}$  drifts from 40 MHz up to  $\sim 40.00082$  MHz over roughly 30 min. Once at thermal equilibrium, the AOM remains stable within  $\pm 50$  Hz, enabling a reliable lock-in frequency reference and minimal filter bandwidth. This stability is crucial for repeatable, high-resolution Brillouin measurements.

## IV. RESULTS

### Instrument sensitivity

We begin by testing the sensitivity of the instrument as a way of defining a performance metric for the instrument which can be used to indicate what material, power, and length combinations might be possible to measure. From Eq. 1, the sensitivity of the instrument is the minimum scattered power,  $P_{\text{Sig}}$ , to produce a sta-

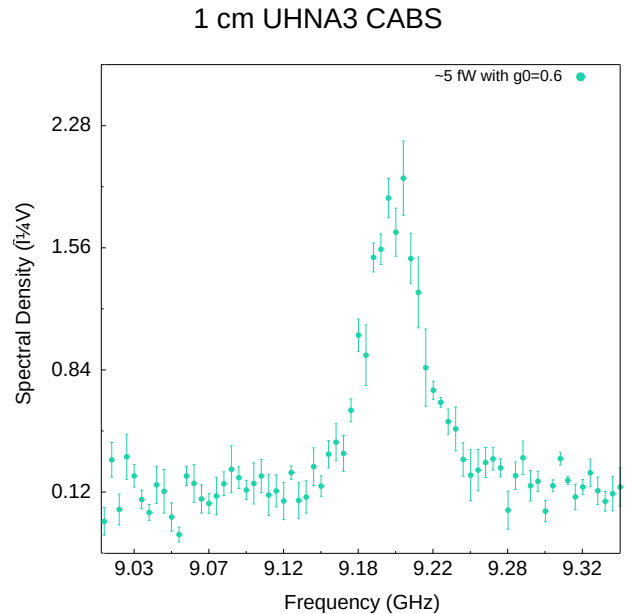


FIG. 3:  $\sim 5$  fW sensitivity measurement

tistically significant measurement. To determine this, we target a specific length,  $L$ , of a sample of known effective Brillouin gain,  $G_B$ . We keep the pump-probe detuning,  $\Delta\lambda$ , constant across measurements and record the pump, Stokes, and probe optical powers to calculate the scattered power. Starting with sufficient optical powers to produce a clearly distinguishable measurement, we gradually reduce the optical powers until the sensitivity floor is reached.

To serve as our sensitivity testbed, we prepared 1 cm of Nufern’s UHNA3 fiber, a well-studied fiber with known effective Brillouin gain[15]. Additionally, UHNA3 fiber offers several properties that make it ideal for this task of unambiguous detection of the Brillouin signal as it diminishes with each subsequent reduction in optical powers. First, it offers a Brillouin shift that is spectrally far from that of the single-mode fiber (SMF28) which constitutes much of the instrument. This ensures that the Brillouin response of the sample is not conflated with the Brillouin response of the instrument itself. Additionally, the core of UHNA3 fiber features a high concentration of germanium which improves the optical and acoustic guidance in the fiber as a result of the large refractive index difference between core and cladding. Finally, UHNA3 fiber offers a high optomechanical nonlinear response, with an effective Brillouin gain of  $0.6 \text{ W}^{-1} \text{ m}^{-1}$  measured at room temperature[15]. This gain factor is larger than that of SMF28 by an order of magnitude[16].

Figure 3 presents a measurement in which the instrument’s sensitivity reaches  $P_{\text{Sig}} = 5$  fW. Each trace is the average of five consecutive scans, and an average of five background scans has been subtracted to isolate the signal. Error bars represent the standard error ( $1\sigma$  of the mean). By comparing the peak amplitude at resonance

1 cm UHNA3 CABS

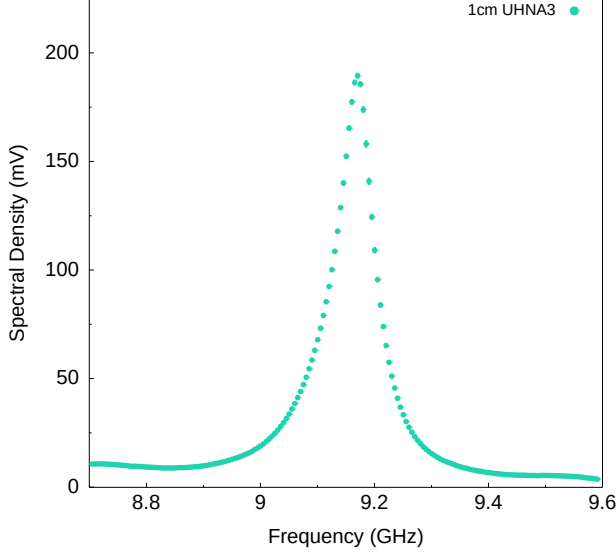
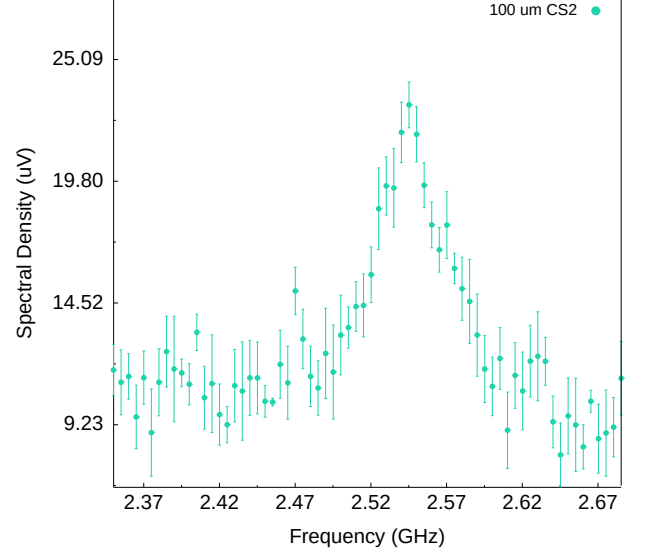


FIG. 4: 1 cm UHNA3

100  $\mu$ m CS<sub>2</sub> CABSFIG. 5: 100  $\mu$ m CS<sub>2</sub>

to the off-resonance baseline, we estimate an SNR greater than 5. Under a normal-noise assumption, an SNR of 5 corresponds to a  $5\sigma$  significance level (99.7% confidence). Achieving this 5 fW threshold demonstrates the feasibility of measuring weaker signals in materials with lower Brillouin gain or smaller effective lengths. Table I in Appendix ?? summarizes the relevant measurement parameters and on-resonance power calculations.

$G_B$ ( $\text{W}^{-1} \text{m}^{-1}$ )	$L$ (m)	$P_P$ ( $\mu\text{W}$ )	$P_S$ ( $\mu\text{W}$ )	$P_{Pr}$ ( $\mu\text{W}$ )	$\Delta\lambda$ (pm)
0.6	0.01	506	504	2.01	20

TABLE I: Measurement parameters for sensitivity measurement and calculation.

### Measurements

We demonstrate the capabilities of the instrument on two common sample classes: fiber and bulk material. For a fiber sample we again choose UHNA3 for its higher non-linear response and excellent optical and acoustic guidance. In contrast to the sensitivity measurements, we now seek to demonstrate the full measuring capabilities of the instrument and so apply all available optical power ( $\sim 1.5 \text{ W}$ ) to maximize the backscattered signal from the sample. We target the same 1 cm segment of UHNA3 fiber as was used for determining sensitivity.

Fig. 4 shows the spectral profile captured for 1 cm of UHNA3 fiber, revealing the expected Lorentzian profile consistent with Eq. 2. The peak amplitude of the spectra occurs at 9.1704 GHz, indicating the Brillouin resonance frequency of the longitudinal traveling-wave mode

in the fiber. The FWHM of the measurement is 80 MHz and provides a measure of the phonon dissipation rate. Both values match what is seen in the literature for SBS measurements of UHNA3 fiber.[15] The data shown are a background-subtracted average of five successive measurements taken over ten minutes with error bars corresponding to  $1\sigma$  of the mean.

To achieve this measurement of UHNA3 fiber, the instrument design was altered to include only fiber-coupled segments connecting the fiber ports between the two PBSs. We set the pump laser wavelength to 1549.000 nm and the probe laser wavelength to 1549.020 nm, giving a frequency mismatch of approximately 2.5 GHz. The pump-probe mismatch is chosen to be only as large as needed to allow the edge of the pass-band of the probe filter to split the backscattered pump and probe light, thus rejecting any backscattered light from the pump laser and accepting only the backscattered signal from the probe laser. We placed the Stokes filter at 1549.073 nm, an offset of approximately 9.18 GHz from the pump laser to capture the Stokes sideband from the intensity modulator. This corresponds to the center of the measured frequency range and was chosen to allow the Stokes sideband output from the intensity modulator to remain within the pass band of the Stokes filter as the RF signal fed to the intensity modulator is swept through the full measurement range. The probe filter was set to 1549.109 nm, an offset of approximately 11.18 GHz from the probe laser, to capture the Stokes-shifted backscattered signal from the probe. The center frequency of the backscattered signal is of course shifted 9.18 GHz from the probe laser, however an extra offset of 2 GHz is chosen for improved rejection of any pump light as the pass band of our filter extends approximately 2.5 GHz on either side of center.



For a free-space bulk example we target liquid  $\text{CS}_2$  for its exceptionally high Brillouin gain factor of  $1.5 \text{ mGW}^{-1}$ . [1] Figure 5 reveals the Brillouin signal of bulk  $\text{CS}_2$  liquid contained in a  $100 \mu\text{m}$  path length cell. To our knowledge, measurement of longitudinal Brillouin scattering at this scale has not been reported in the literature. A scattered power comparison would reveal that achieving such a measurement using traditional SBS techniques would require excessively high optical powers or cooling the material to cryogenic temperatures, which, of course, would be prohibitive for carbon disulfide in the liquid state.

For this measurement of  $\text{CS}_2$ , the pump and probe laser wavelengths were set to  $1548.808 \text{ nm}$  and  $1548.898 \text{ nm}$ , respectively. The short path length of the sample significantly broadens  $\Phi$ , the  $\text{sinc}^2$  term defining the phasematching bandwidth, allowing for further separation of the pump and probe wavelengths for improved signal isolation without significant reduction in scattered power of the signal produced in the  $\text{CS}_2$ . Specifically, the additional pump-probe wavelength separation of  $70 \text{ pm}$  employed for this measurement compared to the UHNA3 measurement results in a negligible  $0.045\%$  reduction in scattered power. This additional separation contributes meaningfully, however, to improved rejection of pump light by the probe filter and thus higher SNR of the signal.

Placement of the Stokes filter is critical for measurements of materials that give small Brillouin shifts, such as with  $\text{CS}_2$   $2.55 \text{ GHz}$  shift. We offset our  $5 \text{ GHz}$  bandwidth Stokes filter an additional  $2 \text{ GHz}$  to ensure the nearby carrier signal and anti-Stokes sideband from the intensity modulator are rejected and only the Stokes sideband is allowed to pass. For the measurement shown in Fig. 5, this corresponds to a Stokes and probe filter placement of  $1548.844 \text{ nm}$  and  $1548.934 \text{ nm}$ , respectively.

### Phase Matching Bandwidth

To characterize the phase matching tolerance of the instrument for a given length of sample, we performed an additional experiment whereby we took a series of measurements of  $1 \text{ cm}$  of UHNA3 at constant optical powers while letting the detuning of the pump and probe lasers vary. In the language of Eq. 1, this experiment holds  $G_B$ ,  $L$ ,  $P_P$ ,  $P_S$ , and  $P_{Pr}$  constant while letting  $\Delta k$  vary. For the experiment to support the validation of Eq. 1, we would expect the peak amplitudes of these measurements to trace out a  $\text{sinc}^2$  profile, also given by Eq. 5. Fig. 6 shows the results of this experiment, in which 75 measurements performed between  $5 \text{ GHz}$  and  $42 \text{ GHz}$  pump-probe frequency separation at  $0.5 \text{ GHz}$  intervals. We found peak amplitudes by fitting each spectra with a Fano profile (see the proceeding *Fano-Resonant Asymmetries at Small Signals* subsection) and are represented by a point in Fig. 6. The theoretical  $\text{sinc}^2$  function for the parameters used in the experiment (listed in Table ?? in

### 1 cm UHNA3 Phase-Matching Bandwidth

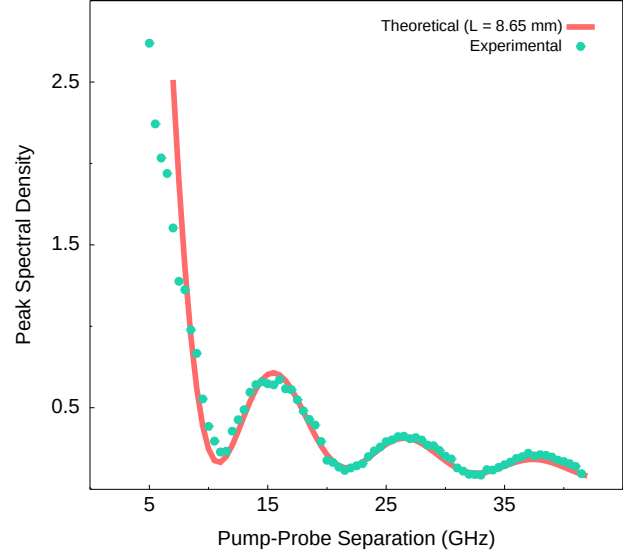


FIG. 6: Phase-matching  $\text{sinc}^2$  func

Appendix ??) is shown on the plot with a solid red line.

### Fano-Resonant Asymmetries at Small Signals

Under certain conditions where the resonant Brillouin amplitude approaches the background continuum level, we observe an asymmetric, Fano-type lineshape [17–20]. These Fano distortions can shift the apparent peak frequency, complicate simple Lorentzian fitting, and affect the extracted linewidth in small-signal measurements. [?] To properly handle these occurrences, it is necessary to understand when they are likely to arise with this technique and how they may be corrected for or controlled. Fano resonances arise when a discrete resonance (in our case, the Brillouin mode) interferes with a continuum background (e.g., noise floor or broad, non-resonant scattering). When the resonance amplitude is no longer much larger than the continuum, the interference leads to an asymmetric lineshape described by the Fano formula [17],

$$I(\omega) \propto \frac{(q + \epsilon)^2}{1 + \epsilon^2}, \quad (6)$$

where  $\epsilon \equiv (\Omega - \Omega_B)/(\Gamma_B/2)$  is the dimensionless detuning from the Brillouin peak (measured in half the spectral linewidth) and  $q$  is the Fano asymmetry parameter.

We first noticed this behavior appearing in our small-length  $\text{CS}_2$  data, where a small shift in probe wavelength revealed an asymmetric lineshape. For the measurements of  $100 \mu\text{m}$   $\text{CS}_2$  (Fig. 5) and  $1 \text{ cm}$  UHNA3 fiber at low power (Fig. 3), the amplitude of the resonant Brillouin peak is on the order of that of the non-resonant continuum, giving a strong chance for Fano interference.

Whenever  $\frac{I_{\text{res}}}{I_{\text{bkg}}} \approx 1$ , the parameter  $q$  can become finite (rather than  $\pm\infty$  in the limit that the background is negligible), and Fano interference arises. To explore this further, we performed a similar phase-matching experiment as was done for 1 cm UHNA3 (see Phase Matching Bandwidth subsection), this time with 1 mm of CS<sub>2</sub>. Results from this are presented in Appendix C and offer a striking example of line shapes with pronounced asymmetry and featuring clear characteristic morphologies associated with various values and signs of  $q$ . These pronounced distortions in spectral line shape for small signal measurements underscore the role of Fano interference in small resonant amplitudes relative to the background.

As our instrument is well suited to measuring samples of length  $< 10$  m and low Brillouin gain, typical signal amplitudes are often small and may sometimes approach the order of the background continuum amplitude. For this reason, Fano effects may more often be present with this technique and must be handled appropriately, such as fitting data with a Fano profile as opposed to a Lorentzian to ensure accurate capture of relevant parameters such as linewidth and peak amplitude. Beyond fitting and parameter extraction, it is important to be mindful that these effects are likely to occur in ambitious measurements at the limits of equipment sensitivity. Expectation and proper handling of Fano effects in measurements of this nature ensures that they may be more easily recognized and confirmed, as the data is likely to present a spectrum that deviates considerably from the standard Lorentzian. In some cases, and of particular interest for ambitious measurements, Fano interference may even *boost* the measured peak above its nominal amplitude—i.e., ‘amplify’ it—when  $q < 0$ . This peak-boosting effect occurs when the scattered Brillouin signal *lags* the background continuum in phase, resulting in a negative  $q$ .

In principle, the Fano lineshape can exhibit a higher peak amplitude than a pure Lorentzian if the discrete Brillouin response interferes constructively with the background near resonance. However, this does not represent net energy gain, since it is an interference effect rather than a true amplification mechanism. Depending on the phase relationship and the background noise level, the observed peak may be taller (enhancing local amplitude), but the net SNR may or may not improve globally, since the background continuum also contributes noise. In any case, our technique permits tuning of the probe wavelength to tailor the phase of the Brillouin signal relative to the background continuum for optimal Fano interference for a given system and measurement. Remarkably, this can be done without giving up independent control of the phase matching bandwidth. This can be achieved through simultaneous adjustment of the pump laser wavelength in step with the probe such that the probe wavelength is Fano-optimized and the desired pump-probe detuning is preserved.

In the phase-matching bandwidth experiment performed on 1 cm UHNA3 (Fig. 6 and described in Phase

Matching Bandwidth subsection), several factors contribute to a slight deviation from the simple theory of a pure sinc<sup>2</sup> function, including noise floor, alignment drifts, fiber dispersion, among possible others. We largely see the sinc<sup>2</sup> dependence, however near the troughs of the sinc<sup>2</sup> function and for greater pump-probe detunings, the measured peaks become quite weak, and a slight spectral asymmetry emerges (see Appendix C). This is consistent with a Fano-type distortion, wherein the signal amplitude is comparable to the underlying continuum, leading to an interference phenomenon that slightly skews the measured peak. Because of the Fano line shape, the peak amplitude from the spectral trace is not exactly at the Lorentzian center and a naive Lorentzian fit would thus not accurately capture the peak amplitude of these greater pump-probe detunings. We corrected for this by fitting a standard Fano profile, which accurately captures the peak amplitudes. Comparing a pure Lorentzian vs. a Fano fit in the limiting data sets indicates that ignoring the Fano effect overestimates the peak amplitude by 5–10%. However, even with a good fit, as described earlier, the Fano-resonant effects serve to amplify or diminish the underlying Brillouin response as a function of the sign of the Fano asymmetry parameter  $q$  for each set (e.g. whether the Brillouin response slightly lags ( $q < 0$ ) or leads ( $q > 0$ ) the broad background continuum in phase, respectively, as determined by the wavelength of the Probe laser).

## V. CONCLUSION

In conclusion, we have introduced a coherently stimulated Brillouin spectrometer utilizing a detuned pump-probe design to achieve high sensitivity and room-temperature operation in  $\mu\text{m}$ -scale samples. This approach successfully overcomes the spatial resolution limitations imposed by conventional SBS methods, demonstrating sub-10 fW sensitivity in UHNA3 fiber and enabling Brillouin measurements in bulk liquid carbon disulfide with unprecedented efficiency. By relaxing phase-matching constraints, this instrument opens new possibilities for characterizing nanoscale material properties and developing nano-acousto-optic devices in standard laboratory settings without the need for cryogenic environments. Moving forward, our methodology could facilitate advancements in high-resolution phonon spectroscopy and inspire further innovations in the study of material mechanics at the microscale, reinforcing the broader applicability of Brillouin-based techniques across materials science, photonics, and sensing technologies.

## ACKNOWLEDGMENTS

The authors acknowledge the developers of the Go programming language (<https://go.dev>) for providing the tools used in data processing and visualization.



Appendix:

A Coherently Stimulated Brillouin Spectrometer

## Appendix A: Coupled-Wave Equations

Here we derive the coupled wave equations that describe coherent stimulated Brillouin scattering involving a pump, Stokes, probe, and backscattered optical field given respectively by

$$\tilde{E}_P(z, t) = A_P e^{i(k_P z - \omega_P t)} + c.c., \quad (A1)$$

$$\tilde{E}_S(z, t) = A_S e^{i(k_S z - \omega_S t)} + c.c., \quad (A2)$$

$$\tilde{E}_{Pr}(z, t) = A_{Pr} e^{i(k_{Pr} z - \omega_{Pr} t)} + c.c., \quad (A3)$$

$$\tilde{E}_{Sig}(z, t) = A_{Sig} e^{i(k_{Sig} z - \omega_{Sig} t)} + c.c., \quad (A4)$$

and a common acoustic field given by

$$\tilde{\rho}(z, t) = \rho_0 + \rho(z, t) e^{i(qz - \Omega t)} + c.c., \quad (A5)$$

where  $\Omega = \omega_P - \omega_S$  and  $q = k_P - k_S = 2k_P$ .

### 1. Acoustic Field

As in the case of SBS[1], we start by assuming that the material obeys the acoustic wave equation,

$$\frac{\partial^2 \tilde{\rho}}{\partial t^2} - \Gamma' \nabla^2 \frac{\partial \tilde{\rho}}{\partial t} - v_s^2 \nabla^2 \tilde{\rho} = \nabla \cdot \vec{f}, \quad (A6)$$

where  $v_s$  is the sound speed in the material and  $\Gamma'$  is a damping parameter given by

$$\Gamma' = \frac{1}{\rho} \left[ \frac{4}{3} \eta_s + \eta_b + \frac{\kappa}{C_p} (\gamma - 1) \right], \quad (A7)$$

where  $\eta_s$  and  $\eta_b$  are the shear and bulk viscosity coefficients of the material, respectively. The source term on the right side of Eq. A6 is the divergence of the electrostrictive force:

$$\vec{f} = \nabla p_{st} = \nabla \cdot \left[ -\frac{1}{2} \epsilon_0 \gamma_e \left( \langle \tilde{E}_P \cdot \tilde{E}_S \rangle + \langle \tilde{E}_{Pr} \cdot \tilde{E}_{Sig} \rangle \right) \right], \quad (A8)$$

which yields, after applying the slowly varying amplitude approximation,

$$\nabla \cdot \vec{f} = \epsilon_0 \gamma_e q^2 (A_P A_S^* + A_{Pr} A_{Sig}^*) e^{i\Delta k z}, \quad (A9)$$

Where  $\Delta k = (k_{Pr} - k_{Sig}) - (k_P - k_S)$  is the phase mismatch between the four optical fields. Only two electrostrictive

terms survive after accounting for the orthogonal polarization of the pump and Stokes fields with respect to that of the probe and backscattered signal. Inserting this electrostrictive force term and the acoustic field (Eq. A5) into Eq. A6, and assuming a slowly varying acoustic amplitude, we find

$$-2i\Omega \frac{\partial \rho}{\partial t} - \Gamma' 2iq^2 \Omega \rho - 2iqv_s^2 \frac{\partial \rho}{\partial z} = \epsilon_0 \gamma_e q^2 (A_P A_S^* + A_{Pr} A_{Sig}^*) e^{i\Delta k z}, \quad (\text{A10})$$

which can be restated in terms of the Brillouin linewidth,  $\Gamma_B = q^2 \Gamma'$ , as

$$-2i\Omega \frac{\partial \rho}{\partial t} - 2i\Omega \Gamma_B \rho - 2iqv_s^2 \frac{\partial \rho}{\partial z} = \epsilon_0 \gamma_e q^2 (A_P A_S^* + A_{Pr} A_{Sig}^*) e^{i\Delta k z}. \quad (\text{A11})$$

Given the phonon dispersion relations  $\Omega_B = |q_B|v_s$  and  $\Omega^2 = q^2 (v^2 - i\Omega \Gamma')$ , Eq. A11 can be rewritten as

$$-2i\Omega \frac{\partial \rho}{\partial t} + (\Omega^2 - \Omega_B^2 - i\Omega \Gamma_B) \rho - 2iqv_s^2 \frac{\partial \rho}{\partial z} = \epsilon_0 \gamma_e q^2 (A_P A_S^* + A_{Pr} A_{Sig}^*) e^{i\Delta k z}. \quad (\text{A12})$$

We take the common assumption that the phonon propagation distance is small compared to the distance over which the source term varies significantly, which allows the spatial derivative term in Eq. A12 to be dropped. We further assume steady-state conditions such that the time derivative term also vanishes, leaving

$$(\Omega_B^2 - \Omega^2 - i\Omega \Gamma_B) \rho = \epsilon_0 \gamma_e q^2 (A_P A_S^* + A_{Pr} A_{Sig}^*) e^{i\Delta k z}. \quad (\text{A13})$$

We thus find the acoustic field amplitude to be

$$\rho(z, t) = \epsilon_0 \gamma_e q^2 \frac{(A_P A_S^* + A_{Pr} A_{Sig}^*) e^{i\Delta k z}}{\Omega_B^2 - \Omega^2 - i\Omega \Gamma_B}. \quad (\text{A14})$$

## 2. Optical Fields

We now turn to the spatial evolution of the optical fields, described by the wave equation,

$$\frac{\partial^2 \tilde{E}_i}{\partial z^2} - \frac{n^2}{c^2} \frac{\partial^2 \tilde{E}_i}{\partial t^2} = \frac{1}{\epsilon_0 c^2} \frac{\partial^2 \tilde{P}_i}{\partial t^2}, \quad (\text{A15})$$

where  $i$  denotes the four optical fields, namely: pump, Stokes, probe, and the backscattered signal. The total nonlinear polarization that gives rise to the source term in the wave equation is given by

$$\tilde{P} = \epsilon_0 \Delta \chi \tilde{E} = \epsilon_0 \Delta \epsilon \tilde{E} = \epsilon_0 \rho^{-1} \gamma_e \tilde{\rho} \tilde{E}. \quad (\text{A16})$$

The parts of  $\tilde{P}$  that can act as phase-matched source terms for the optical fields are

$$\tilde{P}_P = p_P e^{i(k_P z - \omega_P t)} + c.c. = \frac{1}{2} \epsilon_0 \rho_0^{-1} \gamma_e \rho A_S e^{i(k_P z - \omega_P t)}, \quad (\text{A17})$$

$$\tilde{P}_S = p_S e^{i(-k_S z - \omega_S t)} + c.c. = \frac{1}{2} \epsilon_0 \rho_0^{-1} \gamma_e \rho^* A_P e^{i(-k_S z - \omega_S t)}, \quad (\text{A18})$$

$$\tilde{P}_{Pr} = p_{Pr} e^{i(k_{Pr}z - \omega_{Pr}t)} + c.c. = \frac{1}{2} \epsilon_0 \rho_0^{-1} \gamma_e \rho A_{Sig} e^{i(k_{Pr}z - \omega_{Pr}t)} e^{i\Delta kz}, \quad (\text{A19})$$

$$\tilde{P}_{Sig} = p_{Sig} e^{i(-k_{Sig}z - \omega_{Sig}t)} + c.c. = \frac{1}{2} \epsilon_0 \rho_0^{-1} \gamma_e \rho^* A_{Pr} e^{i(-k_{Sig}z - \omega_{Sig}t)} e^{-i\Delta kz}. \quad (\text{A20})$$

Inserting the optical fields (Eqs. A1-A4) and phase-matched source terms (Eqs. A17-A20) into Eq. A15, we obtain

$$\frac{\partial A_P}{\partial z} + \frac{n}{c} \frac{\partial A_P}{\partial t} = \frac{i\omega_P \gamma_e}{2nc\rho_0} \rho A_2, \quad (\text{A21})$$

$$-\frac{\partial A_S}{\partial z} + \frac{n}{c} \frac{\partial A_S}{\partial t} = \frac{i\omega_S \gamma_e}{2nc\rho_0} \rho^* A_P, \quad (\text{A22})$$

$$\frac{\partial A_{Pr}}{\partial z} + \frac{n}{c} \frac{\partial A_{Pr}}{\partial t} = \frac{i\omega_{Pr} \gamma_e}{2nc\rho_0} \rho A_{Sig}, \quad (\text{A23})$$

$$-\frac{\partial A_{Sig}}{\partial z} + \frac{n}{c} \frac{\partial A_{Sig}}{\partial t} = \frac{i\omega_{Sig} \gamma_e}{2nc\rho_0} \rho^* A_{Pr}, \quad (\text{A24})$$

We again assume steady-state conditions, allowing the time derivative term to be dropped. Plugging in the acoustic field amplitude (Eq. A14), we arrive at the coupled-amplitude wave equations for the optical fields,

$$\frac{\partial A_P}{\partial z} = \frac{i\epsilon_0 \omega_P q^2 \gamma_e^2}{2nc\rho_0} \frac{(A_P |A_S|^2 + A_{Pr} A_{Sig}^* A_S) e^{i\Delta kz}}{\Omega_B^2 - \Omega^2 - i\Omega \Gamma_B}, \quad (\text{A25})$$

$$\frac{\partial A_S}{\partial z} = -\frac{i\epsilon_0 \omega_S q^2 \gamma_e^2}{2nc\rho_0} \frac{(|A_P|^2 A_S^* + A_{Pr} A_{Sig}^* A_P) e^{-i\Delta kz}}{\Omega_B^2 - \Omega^2 + i\Omega \Gamma_B}, \quad (\text{A26})$$

$$\frac{\partial A_{Pr}}{\partial z} = \frac{i\epsilon_0 \omega_{Pr} q^2 \gamma_e^2}{2nc\rho_0} \frac{(A_P A_S^* A_{Sig} + A_{Pr} |A_{Sig}|^2) e^{i\Delta kz}}{\Omega_B^2 - \Omega^2 - i\Omega \Gamma_B}, \quad (\text{A27})$$

$$\frac{\partial A_{Sig}}{\partial z} = -\frac{i\epsilon_0 \omega_{Sig} q^2 \gamma_e^2}{2nc\rho_0} \frac{(A_P A_S^* A_{Pr} + |A_{Pr}|^2 A_{Sig}^*) e^{-i\Delta kz}}{\Omega_B^2 - \Omega^2 + i\Omega \Gamma_B}. \quad (\text{A28})$$

We drop the very small signal amplitude terms on the right side of Eqs. A25-A28 and integrate each along the effective length to get the amplitudes,

$$A_P = \frac{i\epsilon_0 \omega_P q^2 \gamma_e^2}{2nc\rho_0} \frac{A_P |A_S|^2}{\Omega_B^2 - \Omega^2 - i\Omega \Gamma_B} \frac{e^{i\Delta kL} - 1}{i\Delta k}, \quad (\text{A29})$$

$$A_S = -\frac{i\epsilon_0\omega_S q^2 \gamma_e^2}{2nc\rho_0} \frac{|A_P|^2 A_S^*}{\Omega_B^2 - \Omega^2 + i\Omega\Gamma_B} \frac{e^{-i\Delta kL} - 1}{-i\Delta k}, \quad (\text{A30})$$

$$A_{Pr} = \frac{i\epsilon_0\omega_{Pr} q^2 \gamma_e^2}{2nc\rho_0} \frac{A_P A_S^* A_{Sig}}{\Omega_B^2 - \Omega^2 - i\Omega\Gamma_B} \frac{e^{i\Delta kL} - 1}{i\Delta k}, \quad (\text{A31})$$

$$A_{Sig} = -\frac{i\epsilon_0\omega_{Sig} q^2 \gamma_e^2}{2nc\rho_0} \frac{A_P A_S^* A_{Pr}}{\Omega_B^2 - \Omega^2 + i\Omega\Gamma_B} \frac{e^{-i\Delta kL} - 1}{-i\Delta k}. \quad (\text{A32})$$

We focus on the signal amplitude given by Eq. A32, noting that close to resonance, the denominator of the middle term containing  $\Omega$  can be approximated as,

$$\Omega_B^2 - \Omega^2 + i\Omega\Gamma_B \approx \Omega_B(\Omega - \Omega_B + i\Gamma_B), \quad (\text{A33})$$

giving

$$A_{Sig} = -\frac{i\epsilon_0\omega_{Sig} q^2 \gamma_e^2}{2nc\rho_0} \frac{A_P A_S^* A_{Pr}}{\Omega_B(\Omega - \Omega_B + i\Gamma_B)} \frac{e^{-i\Delta kL} - 1}{-i\Delta k}, \quad (\text{A34})$$

and in fact on resonance the expression reduces to

$$A_{Sig} = -\frac{i\epsilon_0\omega_{Sig} q^2 \gamma_e^2}{2nc\rho_0} \frac{A_P A_S^* A_{Pr}}{\Omega_B i\Gamma_B} \frac{e^{-i\Delta kL} - 1}{-i\Delta k}. \quad (\text{A35})$$

Using  $q = 2k_P = 2\omega n/c$  and  $q = \Omega_B/v_s$ , we can express the leading terms as

$$A_{Sig} = -\frac{\epsilon_0\omega^2 \gamma_e^2}{c^2 v_s \rho_0 \Gamma_B} A_P A_S^* A_{Pr} \frac{e^{-i\Delta kL} - 1}{-i\Delta k}, \quad (\text{A36})$$

where we have dropped the signal designator on  $\omega$ . Defining the Brillouin gain factor,  $g_0$ , as Boyd does,

$$g_0 = \frac{\gamma_e^2 \omega^2}{nvc^3 \rho_0 \Gamma_B}, \quad (\text{A37})$$

reduces this expression to

$$A_{Sig} = -\epsilon_0 n c g_0 A_P A_S^* A_{Pr} \frac{e^{-i\Delta kL} - 1}{-i\Delta k}. \quad (\text{A38})$$

The intensity of the backscattered signal is given by the magnitude of the time-averaged Poynting vector, given by

$$I_i = 2n\epsilon_0 c |A_i|^2, \quad i = 1, 2, 3, \dots \quad (\text{A39})$$

which produces for the signal intensity

$$I_{Sig} = 2\epsilon_0 n c (\epsilon_0 n c g_0)^2 |A_P|^2 |A_S^*|^2 |A_{Pr}|^2 \left| \frac{e^{-e\Delta k L} - 1}{-i\Delta k} \right|^2 = 2\epsilon_0^3 \epsilon_0 n^3 c^3 g_0^2 \frac{I_P}{2\epsilon_0 n c} \frac{I_S}{2\epsilon_0 n c} \frac{I_{Pr}}{2\epsilon_0 n c} \left| \frac{e^{-e\Delta k L} - 1}{-i\Delta k} \right|^2. \quad (A40)$$

The squared modulus term containing  $\Delta k$  can be reduced as

$$\begin{aligned} \left| \frac{e^{-i\Delta k L} - 1}{-i\Delta k} \right|^2 &= \frac{(e^{-i\Delta k L} - 1)(e^{i\Delta k L} - 1)}{(\Delta k)^2} = \frac{L^2}{(\Delta k L)^2} \left[ 2 - 2 \left( \frac{e^{i\Delta k L} + e^{-i\Delta k L}}{2} \right) \right] \\ &= \frac{2L^2(1 - \cos \Delta k L)}{(\Delta k L)^2} = \frac{4L^2 \sin^2\left(\frac{\Delta k L}{2}\right)}{(\Delta k L)^2} = \frac{L^2 \sin^2\left(\frac{\Delta k L}{2}\right)}{\left(\frac{\Delta k L}{2}\right)^2} = L^2 \text{sinc}^2\left(\frac{\Delta k L}{2}\right), \end{aligned} \quad (A41)$$

giving as a final expression for backscattered signal intensity,

$$I_{Sig} = \frac{1}{4} (g_0 L)^2 I_P I_S I_{Pr} \text{sinc}^2\left(\frac{\Delta k L}{2}\right). \quad (A42)$$

To find the power of the backscattered signal, we would integrate this intensity over the effective area. For a uniform area  $A_{eff}$ , this gives

$$P_{Sig} = I_{Sig} A_{eff} = \frac{1}{4} (g_0 L)^2 \frac{A_{eff}}{A_{eff}} I_P \frac{A_{eff}}{A_{eff}} I_S \frac{A_{eff}}{A_{eff}} I_{Pr} \text{sinc}^2\left(\frac{\Delta k L}{2}\right) A_{eff}, \quad (A43)$$

or,

$$P_{Sig} = \frac{1}{4} (G_B L)^2 P_P P_S P_{Pr} \text{sinc}^2\left(\frac{\Delta k L}{2}\right), \quad (A44)$$

where,

$$G_B = \frac{g_0}{A_{eff}}. \quad (A45)$$

We can also see that off resonance, the  $\Omega$  term from Eq. A34 goes to a lorentzian form after taking the squared modulus for intensity.



## Appendix B: Scattered Power Comparison to Traditional Brillouin Scattering Processes

This appendix provides a comparative analysis of the scattered power produced by our instrument to that of standard Brillouin scattering processes—that is, spontaneous and stimulated Brillouin scattering. The difference in behavior of our instrument from the traditional techniques arises due to the coherent stimulation of the acoustic mode by the pump and Stokes fields, producing a 4-wave-coupled-amplitude interaction that yields much higher scattered powers in smaller lengths. While our instrument is particularly well suited to small interaction lengths due to enhanced phase-matching relaxation, it maintains production of a significant amount of scattered power at greater lengths as well (greater than 1 m). This is because the reduction in scattered power from the breakdown of phase-matching relaxation at greater lengths is perfectly counter-balanced by the quadratic dependence on length in the overall scattered power, as seen in Eq. 1. At very large lengths (greater than 1 km), the instrument is ultimately limited by the coherence length of the lasers employed, as the process relies on the coherent stimulation of the phonon mode and thus the mutual coherence of the pump and Stokes fields over the interaction length. Here we offer an exploration into the respective performance of each technique across the entire meaningful length scale, from nanometers to kilometers.

Despite shared dependence on basic Brillouin scattering principles, the three techniques compared here (spontaneous-, stimulated-, and coherently stimulated Brillouin scattering) yield significantly different scattered power for identical experimental parameters. At small lengths, the high-gain threshold for optical stimulation of the material fluctuations is often not achievable without the use of extremely large optical powers. This prevents the system from entering a process of exponential growth of the scattered Stokes light indicative of stimulated Brillouin scattering.[1] In this low-gain regime, any scattered Stokes light is spontaneously scattered from thermal fluctuations of the material, or from quantum-mechanical fluctuations of materials at the ground state. The low-gain regime is defined by an overall process gain factor, denoted by  $G = G_P P_P L$ , which is much less than unity ( $G \ll 1$ ). Here,  $G_B$  is the effective Brillouin gain in  $\text{W}^{-1} \text{m}^{-1}$  ( $G_B = \frac{g}{A_{eff}}$ ),  $P_P$  is the pump power, and  $L$  is the effective length. This spontaneous scattering process follows a linear growth trend described by Boyd et al in 1990[21] as

$$R = \frac{\langle |E_S|^2 \rangle}{\langle |E_P|^2 \rangle} = (\bar{n} + 1) g \hbar \omega_S \Gamma_B \frac{L}{4A_{eff}}, \quad (\text{B1})$$

where  $R$  is the reflectivity, or the ratio of scattered Stokes intensity to incident pump intensity, and  $\bar{n} = (e^{\frac{\hbar \Omega_B}{k_b T}} - 1)^{-1}$  is the mean number of phonons occupying the mode due to thermal fluctuations of the material. Rearranging this equation and converting to effective Brillouin gain,  $G_B$ , and power by applying the effective area, we arrive at the scattered power of the Stokes spontaneous Brillouin scattering process,

$$P_S = \frac{1}{4} G_B P_P L \hbar \omega_S \Gamma_B (\bar{n} + 1). \quad (\text{B2})$$

At room temperature and typical Brillouin frequencies in the GHz range, the quantity  $k_b T \gg \hbar \Omega_B$ , allowing

$$e^{\frac{\hbar \Omega_B}{k_b T}} \approx 1 + \frac{\hbar \Omega_B}{k_b T} \quad (\text{B3})$$

to be a good approximation. We thus find that

$$(\bar{n} + 1) \approx \bar{n} \approx \frac{k_b T}{\hbar \Omega_B}. \quad (\text{B4})$$

Inserting this reduced quantity into Eq. B2, we arrive at a convenient expression for the scattered power of the Stokes spontaneous Brillouin scattering process,

$$P_{S, \text{SponBS}} = \frac{G_B P_P L \omega_S \Gamma_B k_b T}{4 \Omega_B}. \quad (\text{B5})$$

It may be noted that the derived expression for the low-gain spontaneous regime here matches the form reported by Kharel et al. in 2016[22] for the complementary forward scattering process. While the two scenarios—our backward scattering geometry versus the forward scattering geometry discussed by Kharel et al.—differ in directionality, the

underlying physics of light coupling to thermally excited acoustic modes is the same and reflects the fundamental similarity in how thermal phonons mediate the interaction between optical fields in the low-gain (spontaneous) regime.

Next we turn to the high-gain regime leading to a stimulated Brillouin scattering process. This regime is defined by an overall process gain factor,  $G = G_P P_P L$ , that is much greater than unity ( $G \gg 1$ ). For organic liquids, this crossover threshold from spontaneous to stimulated regimes occurs in the range of  $20 < G < 25$ , [21] whereas for typical lengths of single mode fiber it can be lower [5] owing to the small effective area compared to longer effective lengths of fiber typically used.

The reflectivity of a stimulated Brillouin scattering process in the high-gain regime is given by [21]

$$R = \frac{\langle |E_S|^2 \rangle}{\langle |E_P|^2 \rangle} = \frac{Y}{\sqrt{\pi}} \frac{e^G}{G^{\frac{3}{2}}}, \quad (\text{B6})$$

where  $Y$  is the reflectivity of the low-gain (spontaneous) regime given above and  $G$  is the overall process gain factor,  $G = G_P P_P L$ . Again, converting to the effective Brillouin gain,  $G_B$ , and power by applying the effective area, we solve for the scattered power of the Stokes field,

$$P_{S, \text{StimBS}} = \frac{G_B P_P L \omega_S \Gamma_B k_b T}{4\sqrt{\pi} \Omega_B} \frac{e^G}{G^{\frac{3}{2}}} \quad (\text{B7})$$

This expression captures the exponential growth in scattered power as any parameter within the overall process gain factor,  $G = G_B P_P L$ , increases. However, this exponential growth can only continue while the pump is not significantly undepleted. Once the scattered power described by Eq. B7 grows to a significant fraction of the driving pump power, the exponential increase in scattered Stokes power asymptotically approaches the pump power. For very large  $G$ , virtually all of the pump energy is converted to scattered Stokes energy in a complete transfer process. [1] To account for pump depletion, we numerically solve the transcendental equation derived in Boyd's Nonlinear Optics which describes the effects of pump depletion, given here in terms of power as

$$P_S(L) = \frac{P_S(0)x(1-x)}{e^{G_B P_P(0)L(1-x)} - x}, \quad (\text{B8})$$

where  $x = P_S(0)/P_P(0)$ , or the ratio of the unknown Stokes power at the end of its journey through the medium ( $z = 0$ ) to the known pump power at the beginning (also  $z = 0$ ). This solution for  $x$ , specific to system parameters such as length, offers via its definition the solution to the unknown power of the scattered Stokes light at the end of its traversal through the effective length, given as

$$P_S(0) = x P_P(0). \quad (\text{B9})$$

The solution to this numeric approach to scattered power in the high-gain (stimulated) Brillouin scattering regime with pump depletion effects at large  $G$  is plotted for varying effective lengths in Fig. 7, along with the analytical solutions derived previously for the low-gain (spontaneous) regime and our coherently stimulated Brillouin spectrometer given by Eq. 1. System parameters used to generate the plot for each of the three processes are provided in Tables II and III. Wherever possible, the parameters shared by all three Brillouin scattering processes were kept consistent, while quantities unique to each process were assigned their respective values.

**Coherently Stimulated Brillouin Scattering Process Model System Parameters**

$G_B$	$P_P$	$P_S$	$P_{Pr}$	$\Delta\lambda$
$0.6 \text{ W}^{-1} \text{ m}^{-1}$	1 W	1 W	1 W	20 pm

TABLE II: Parameters relevant to the coherently stimulated backward Brillouin scattering process for the example UHNA3 fiber.  $G_B$  is the effective Brillouin gain,  $P_P$  is the pump power,  $P_S$  is the Stokes power,  $P_{Pr}$  is the probe power, and  $\Delta\lambda$  is the wavelength detuning of the probe from the pump.

At lengths beyond a centimeter, the phase-matching relaxation of the coherently stimulated process begins to break down, and the specific choice in pump and probe detuning becomes critical. This corresponds to a narrowing of the  $\text{sinc}^2$  function given in Eq. 5. The scattered power beyond this length rises and falls according to the oscillations of the  $\text{sinc}^2$  function far from the origin. As length increases continuously beyond 1 meter, the scattered power oscillates

**Spontaneous and Stimulated Scattering Process Model System Parameters**

$G_B$	$P_P$	$P_{S,seed}$	$n$	$\lambda_P$	$\Gamma_B$	$k_B$	$T$	$\Omega_B$
$0.6 \text{ W}^{-1} \text{ m}^{-1}$	1 W	1 pW	1.48	1549 nm	$2\pi \cdot 80 \text{ MHz}$	$1.38 \times 10^{-23} \text{ J K}^{-1}$	295 K	$2\pi \cdot 9.18 \text{ GHz}$

TABLE III: Parameters relevant to the spontaneous and/or stimulated backward Brillouin scattering processes for the example UHNA3 fiber.  $G_B$  is the Brillouin gain coefficient,  $P_P$  is the pump power,  $\omega$  is the optical angular frequency,  $\Gamma_B$  is the acoustic damping rate,  $k_B$  is Boltzmann's constant,  $T$  is the temperature, and  $\Omega_B$  is the acoustic angular frequency.

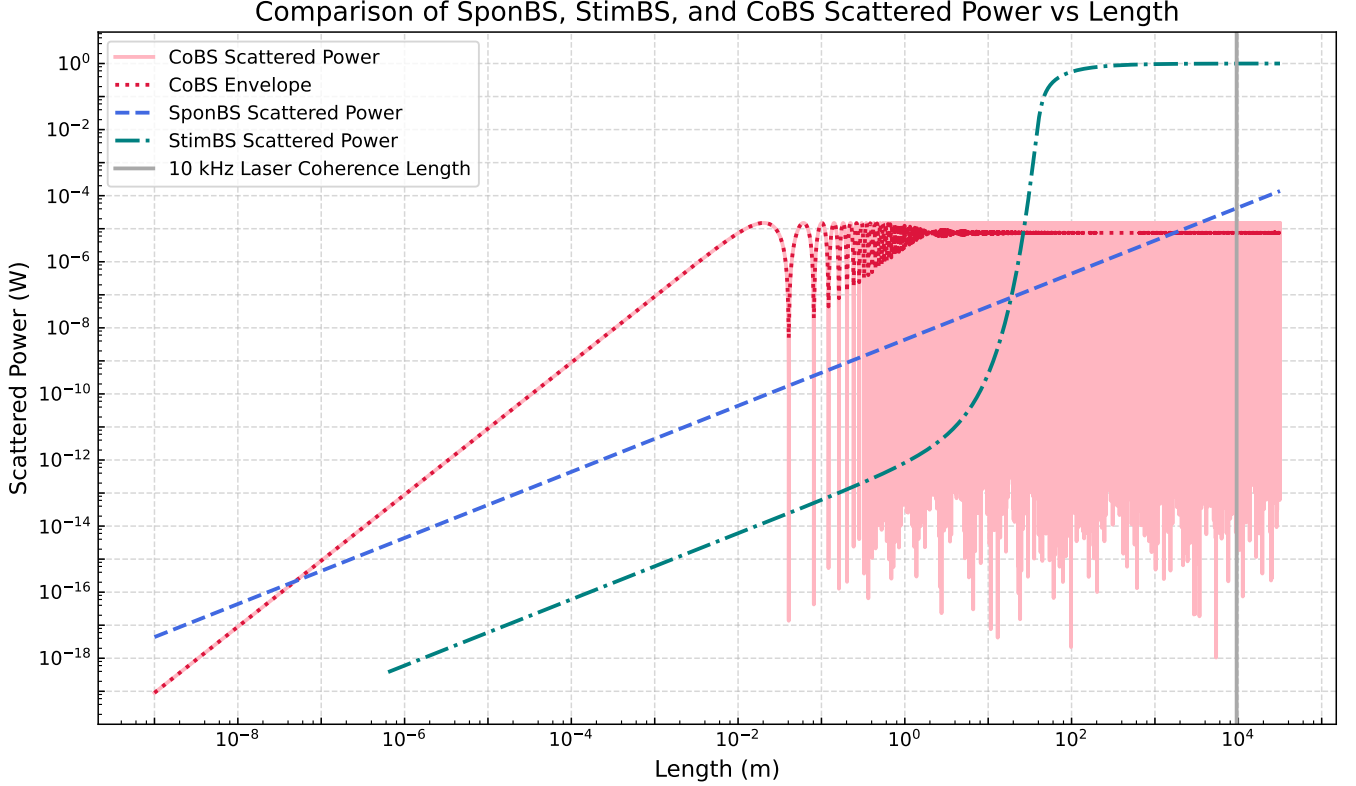


FIG. 7: Comparison of scattered power from a spontaneous Brillouin scattering process and our coherently stimulated Brillouin spectrometer.

with increasing frequency and ceases to offer practical significance. To better visualize the scattered power offered by the instrument in this region, we have computed the envelope of scattered power. In a laboratory setting, the appropriate pump and probe detuning would be selected for the specific sample length being measured such that the scattered power function lies on a local peak of the  $\text{sinc}^2$  function.

Fig. 7 shows the advantage that our coherently stimulated Brillouin spectrometer offers compared to the traditional Brillouin processes for the example medium of UHNA3 fiber. For lengths up to about 50 m and down to as low as 100 nm, the coherently stimulated process employed by our instrument offers superior scattered power, with the relative advantage peaking for a length just over 1 cm. At this length, the gain factor  $G$  places the traditional process within the low-gain (spontaneous) regime, and thus the scattered power generated is only on the order of tens of pW. In contrast, the scattered power offered by our instrument for the same system and identical powers is on the order of tens of  $\mu\text{W}$ , exceeding that of the spontaneous process by a factor of  $10^6$ . This is, of course, the most ideal case for this system, however it can be seen from Fig. 7 that the coherently stimulated process offers orders of magnitude more scattered power than either traditional process through a wide range of lengths.

## Appendix C: Observance of Fano-Resonant Asymmetries at Small Signals

In the main text (*Fano-Resonant Asymmetries at Small Signals* in Sec. IV), we discussed how Fano-type interference can distort Brillouin line shapes in situations where the resonant Brillouin amplitude becomes comparable to the background continuum. We focus here on two experiments (A and B) that reveal these Fano asymmetries especially clearly. Experiment A is a measurement series using the same 1 cm UHNA3 fiber referenced in the main discussion, for which the main text showed only the fitted amplitudes (Fig. 6). Here we show the full spectra, illustrating the emergence of asymmetries at lower amplitude conditions. Experiment B is a distinct measurement involving a short ( $\sim 1$  mm) bulk liquid sample of carbon disulfide ( $\text{CS}_2$ ) that we briefly mentioned in Sec. IV but did not detail. This experiment was performed specifically to further probe the unexpected Fano-like distortions observed in Experiment A. In each case, we outline the experimental setup, present the spectra, and highlight the appearance of Fano resonances. These observations corroborate the theoretical discussion of Fano line shapes (Sec. IV) and provide insight into when and why they are most prominent.

### 1. Experiment A: Extended 1 cm UHNA3 Fiber Spectra

In the main text, we introduced a phase-matching experiment on 1 cm of UHNA3 fiber in which the pump-probe detuning was varied from 5 GHz to 42 GHz in 0.5 GHz increments. There, we reported only the resulting peak amplitudes, showing how they follow a  $\text{sinc}^2$  dependence on detuning (Fig. 6 in the main text). However, each measurement in that scan also yields a full Brillouin spectrum—75 in total. Here, we present selected spectra to illustrate how the line shape transitions from nearly Lorentzian (when the Brillouin peak amplitude greatly exceeds the background continuum) to distinctly Fano-like (when the two amplitudes are comparable).

We used the same setup and procedure described in *Phase Matching Characterization* in Sec. IV of the main text. As the pump-probe detuning increases, the phase-matching term  $\text{sinc}^2(\Delta k L/2)$  oscillates through peaks and troughs, causing the Brillouin peak amplitude to rise and fall. When the amplitude is sufficiently large, the Brillouin mode dominates the continuum and the spectrum appears nearly Lorentzian; when it drops to the order of the background amplitude, strong interference skews the line shape into a Fano-like profile.

FIG. 8: Representative Brillouin spectra for 1 cm UHNA3 at different pump-probe detunings, selected to illustrate the transition from Lorentzian-like peaks ( $q \rightarrow \infty$ ) to strongly Fano-distorted profiles ( $q$  finite). Spectra have been normalized by optical power and offset vertically for clarity.

Figure 8 highlights the progressive shift from Lorentzian to asymmetric line shapes. Near 5 GHz detuning, the resonant amplitude is large relative to the background, giving a classic Lorentzian peak at  $\sim 9.17$  GHz. By contrast, at detunings between  $\sim 15$ –20 GHz (where the  $\text{sinc}^2$  factor is near a local minimum), the peak amplitude falls to roughly the same level as the continuum, and the Fano interference is obvious. Interestingly, as the detuning continues to climb, the amplitude rises again on a subsequent  $\text{sinc}^2$  “lobe,” and the spectra partly recover a Lorentzian shape. This cyclical behavior persists, with each local maximum yielding a near-Lorentzian profile and each local minimum reintroducing a strong Fano distortion.

These observations confirm the relationship between Brillouin peak amplitude and continuum interference described in *Fano-Resonant Asymmetries at Small Signals* in Sec. IV. When the Brillouin amplitude significantly exceeds the background, the discrete phonon resonance dominates, resulting in little or no asymmetry ( $q \rightarrow \pm\infty$ ). Once the two amplitudes become comparable, Fano interference skews the line shape, shifting the apparent peak frequency slightly and altering the slope on one side of the resonance. Analyzing selected spectra with both Lorentzian and Fano fits indicates that ignoring these distortions can lead to up to a 5–10% misestimation of peak amplitude in the “trough” (low-amplitude) sets. This underscores the importance of employing a Fano model—particularly in small-signal measurements where the Brillouin peak may not tower over the background.

### 2. Experiment B: 1 mm $\text{CS}_2$ Spectra and Fano Distortions

We now turn to measurements on a 1 mm-thick cell of  $\text{CS}_2$  in a free-space geometry, complementing the 1 cm UHNA3 fiber results (Experiment A). Both experiments used comparable sub-Watt optical powers (on the order of  $\sim 60$ –70 mW pump,  $\sim 25$ –30 mW Stokes, and  $\sim 40$ –50 mW probe). However, unlike Experiment A—which probed a 1 cm fiber with 0.5 GHz detuning increments from 5 GHz to 42 GHz—here the detuning is stepped in 0.25 GHz increments between 10 GHz and 14 GHz. Because the  $\text{CS}_2$  sample is an order of magnitude shorter (1 mm vs. 1 cm), its phase-matching

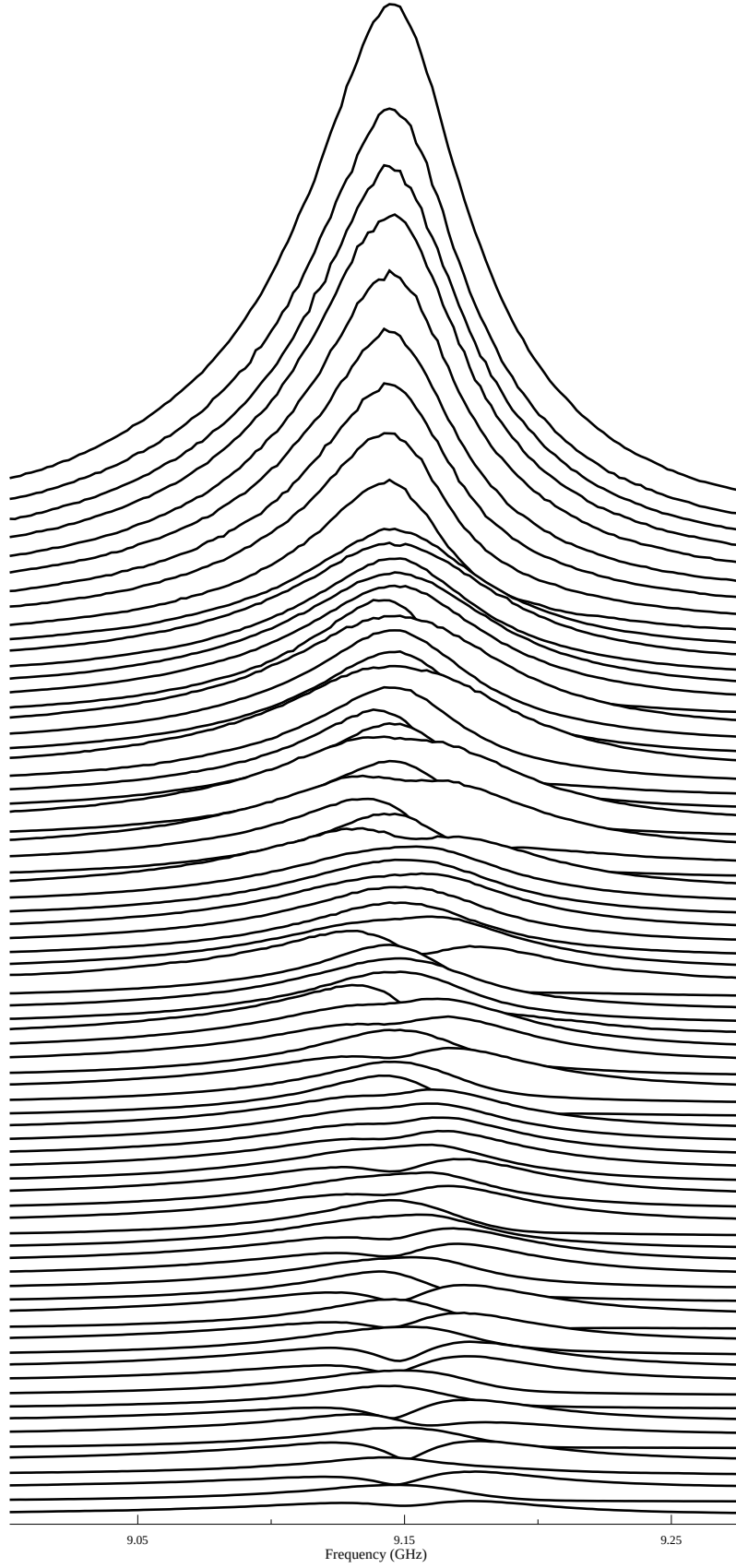


FIG. 9: Stacked Brillouin spectra showing Fano-type line-shape distortions at small signals in a 1 cm UHNA3 fiber. Each trace corresponds to a different pump-probe detuning, revealing the discrete Brillouin resonance (near 9.17 GHz) interfering with a broad continuum background. The resulting asymmetries highlight the characteristic Fano resonant behavior under low signal conditions.

bandwidth ( $\text{sinc}^2$  profile) is roughly ten times wider, making these 0.25 GHz steps effectively twenty times finer than the 0.5 GHz steps used in the fiber experiment. This reduced range of detunings within a broader  $\text{sinc}^2$  profile produce measured peaks all of similar amplitude to one another, as opposed to the dynamic evolution of peaks in the 1 cm UHNA3 fiber data.

Figure 10 shows all 17 spectra obtained at detuning increments of 0.25 GHz. Each trace is offset vertically for clarity, and the legend indicates the central detuning from 10 GHz to 14 GHz. A change in the detuning of the pump and probe via adjustment of the probe laser wavelength produces a change in phase of the resonant Brillouin signal. This changing resonant Brillouin phase relative to the background continuum produces spectra with different Fano-resonant distortions corresponding to specific values of the Fano parameter  $q$ , as discussed in *Fano-Resonant Asymmetries at Small Signals* (Sec. IV). Fano-asymmetries are seen in every spectrum of this liquid experiment, indicating that the background continuum is competing strongly with the Brillouin amplitude in all measurements despite the advantage of broadened phase matching bandwidth. This lower Brillouin amplitude is owing to the order of magnitude shorter sample length and roughly two orders of magnitude larger effective area in our free-space configuration compared to that of the UHNA3 fiber in Experiment A.

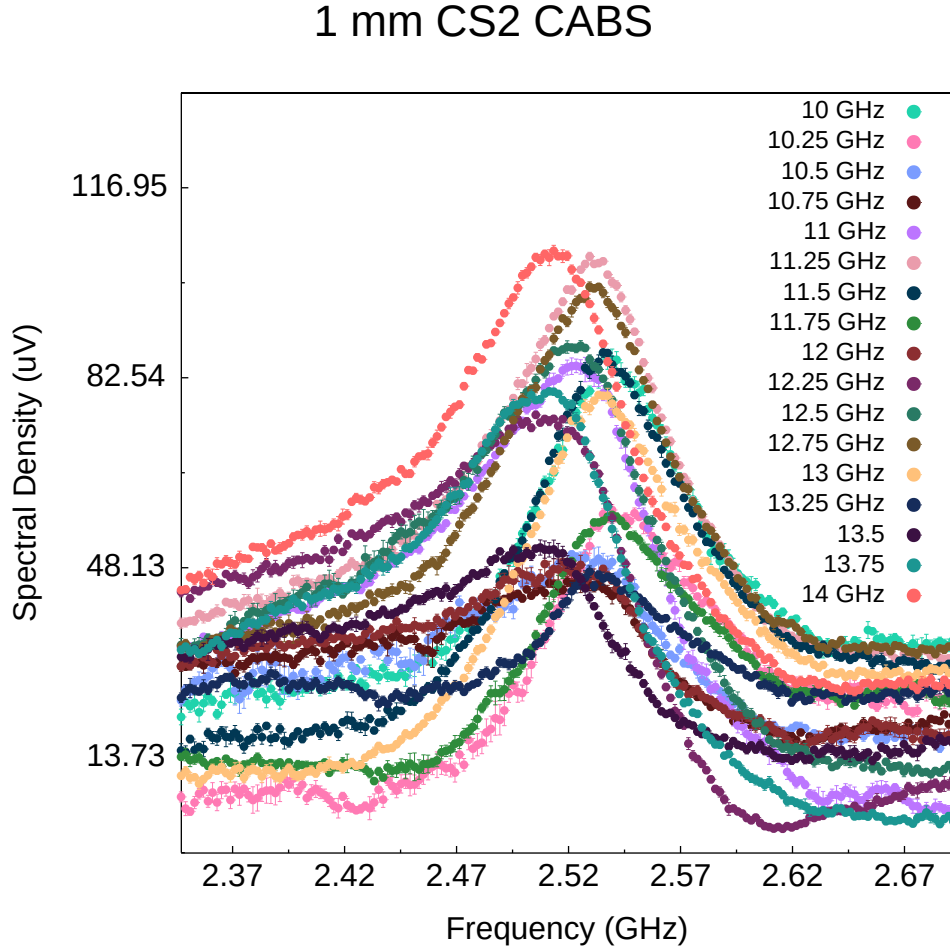


FIG. 10: All measured Brillouin spectra for 1 mm  $\text{CS}_2$  at detuning steps of 0.25 GHz from 10 GHz to 14 GHz. Each trace is offset for clarity. The vertical scale is in arbitrary units of spectral density after background subtraction.

To illustrate how the Fano asymmetry parameter  $q$  can be positive or negative, we focus on two particular detunings that yielded notably skewed line shapes: 10.75 GHz and 13.5 GHz. Figure 11 compares the spectra for these two detunings, overlaid with both a Lorentzian fit (dashed lines) and a Fano fit (solid lines). The insets show residuals (data minus fit). The measured peak of the 13 GHz spectrum (Fig. 11b) exhibits a sharper rise on the lower-frequency side and a gentler roll-off on the higher-frequency side, indicative of  $q > 0$ , whereas that of the 13.75 GHz spectrum is skewed in the opposite sense, featuring a sharper high-frequency side and a softer low-frequency slope, suggesting  $q < 0$ . Clearly, the Fano model captures the asymmetric tails better than a simple Lorentzian, especially around the half-maximum slopes.



Notably, in the negative- $q$  case (13.75 GHz), the line’s peak amplitude appears slightly higher than what would be inferred from a Lorentzian fit—sometimes referred to as a “peak boost.” As discussed in *Fano-Resonant Asymmetries at Small Signals* (Sec. IV), this can be beneficial for detecting weaker signals, provided the background is not too noisy, and in principle, one could choose a phase relationship that maximizes this constructive interference near resonance. Conversely, a positive- $q$  scenario can suppress or broaden the peak on one side, which may be less desirable for line-shape analysis but could be exploited if one aims to shape the response profile in a particular way.

(a) Representative spectrum at 13 GHz, illustrating positive  $q$  asymmetry. Dashed lines are Lorentzian fits; solid lines are Fano fits. Residuals in the inset highlight the improved agreement of the Fano model.

(b) Representative spectrum at 13.75 GHz, illustrating negative  $q$  asymmetry. Dashed lines are Lorentzian fits; solid lines are Fano fits. Residuals in the inset highlight the improved agreement of the Fano model.

FIG. 11: Comparison of representative spectra at (a) 13 GHz and (b) 13.75 GHz, showing the positive vs. negative  $q$  asymmetry in 1 mm CS<sub>2</sub>. Residuals in the insets highlight the improved agreement of the Fano model over the Lorentzian model.

These 1 mm CS<sub>2</sub> data reinforce the conclusions from the UHNA3 fiber measurements, demonstrating that Fano-type asymmetries arise readily in small-signal regimes across diverse geometries (liquid cell vs. fiber). Moreover, we have explicitly identified positive- and negative- $q$  cases, showing that interference can either boost or clip the Brillouin resonance peak, depending on the sign of  $q$  and the relative amplitude of the background continuum. As in Experiment A, a Fano-fitting procedure is essential to extract accurate linewidths and center frequencies in these small-signal conditions.

To better convey the cyclical evolution of the 75 measured UHNA3 spectra from Experiment A, we have created an animated GIF that steps through each spectrum in ascending pump–probe detuning. This animation can be found in the Supplemental Material as a separate file. We also host the GIF (along with the raw data, measurement logs, and plotting scripts) in a public GitHub repository:

<https://github.com/HamletTheHamster/A-Coherently-Stimulated-Brillouin-Spectrometer>

Readers are encouraged to view it for a clear, dynamic perspective on how the line shape transitions between Lorentzian and Fano-distorted forms at different detunings.

### Appendix D: Pump, Stokes, and Probe Contribute Equally

Eq. 1 gives the somewhat unintuitive result that the powers of the Pump, Stokes, and Probe waves contribute equally to the resulting scattered power of the Signal and invites verification with a miniexperiment. Initially, this experiment was motivated by a practical consideration: determination of whether the placement of a high power amplifier on any specific line of the setup (Pump, Stokes, or Probe) would offer any advantage over another.

To test this, we conducted a controlled experiment with a 1 mm carbon disulfide ( $\text{CS}_2$ ) sample. For each measurement, one of the three source powers (Pump, Stokes, or Probe) was systematically reduced by 75% while holding the others constant and ensuring consistent experimental conditions across trials. Table IV shows the respective powers for each source during the three measurements, along with the multiplicative total contribution of the three powers for each measurement towards the generation of scattered power of the Signal.

Measurement	Pump Power (mW)	Stokes Power (mW)	Probe Power (mW)	Total ( $\text{mW}^3$ )
Pump Lower	19.190	32.210	54.560	$3.372 \times 10^4$
Stokes Lower	76.600	8.020	54.650	$3.359 \times 10^4$
Probe Lower	76.600	32.530	13.480	$3.359 \times 10^4$

TABLE IV: Power values for each source (Pump, Stokes, Probe) across the three measurements, with the multiplicative total power for each setup.

Figure 12a displays the average results from these three measurements, plotted with error bars representing one standard deviation of the mean. For increased certainty, Figure 12b presents the same data with error bars extended to two standard deviations, providing additional confidence in the reproducibility of the results. This experiment confirms that the scattered Signal power indeed depends equally on each of the three contributing wave powers, as expected from the theoretical framework. Consequently, boosting the power of any of the three sources affects the Signal power equally, allowing flexibility in pragmatic design across any of the three lines. Ultimately, this result reinforces the reliability of Equation 1 for predicting Signal power across a range of power distributions within practical settings.

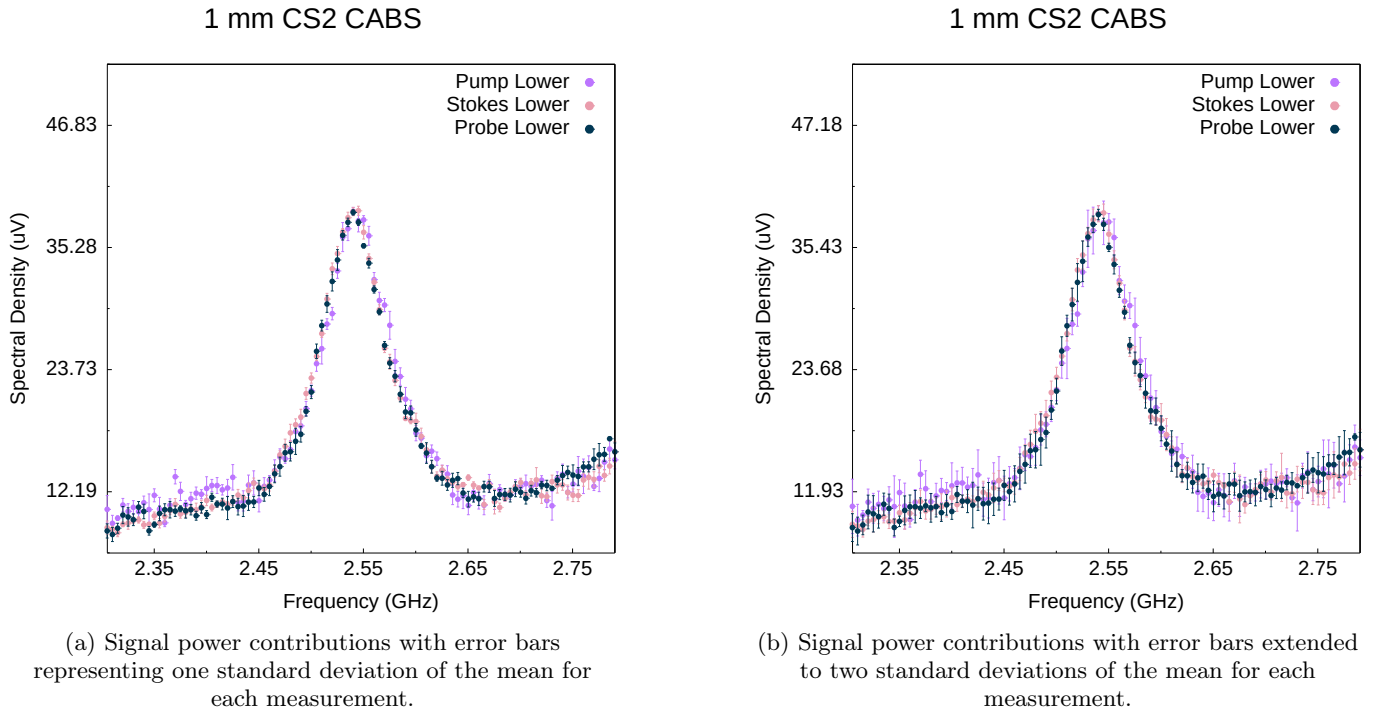


FIG. 12: Comparison of Signal power contributions with error bars representing one (a) and two (b) standard deviations of the mean for each measurement.

- 
- [1] R. W. Boyd, *Nonlinear Optics* (Academic Press, 2020).
  - [2] B. J. Eggleton, C. G. Poulton, and R. Pant, Inducing and harnessing stimulated brillouin scattering in photonic integrated circuits, *Advances in Optics and Photonics* **5**, 536 (2013).
  - [3] A. Fotiadi, D. Korobko, and I. Zolotovskii, Brillouin lasers and sensors: Trends and possibilities, *Optoelectronics, Instrumentation and Data Processing* **59**, 66 (2023).
  - [4] A. Kobayakov, M. Sauer, and D. Chowdhury, Stimulated brillouin scattering in optical fibers, *Advances in optics and photonics* **2**, 1 (2009).
  - [5] E. Ippen and R. Stolen, Stimulated brillouin scattering in optical fibers, *Applied Physics Letters* **21**, 539 (1972).
  - [6] P. T. Rakich, C. Reinke, R. Camacho, P. Davids, and Z. Wang, Giant enhancement of stimulated brillouin scattering in the subwavelength limit, *Physical Review X* **2**, 011008 (2012).
  - [7] F. Gyger, J. Liu, F. Yang, J. He, A. S. Raja, R. N. Wang, S. A. Bhave, T. J. Kippenberg, and L. Thévenaz, Observation of stimulated brillouin scattering in silicon nitride integrated waveguides, *Physical review letters* **124**, 013902 (2020).
  - [8] H. Shin, W. Qiu, R. Jarecki, J. A. Cox, R. H. Olsson, A. Starbuck, Z. Wang, and P. T. Rakich, Tailorable stimulated brillouin scattering in nanoscale silicon waveguides, *Nature communications* **4**, 1 (2013).
  - [9] R. Van Laer, B. Kuyken, D. Van Thourhout, and R. Baets, Interaction between light and highly confined hypersound in a silicon photonic nanowire, *Nature Photonics* **9**, 199 (2015).
  - [10] E. A. Kittlaus, H. Shin, and P. T. Rakich, Large brillouin amplification in silicon, *Nature Photonics* **10**, 463 (2016).
  - [11] R. Pant, E. Li, D.-Y. Choi, C. Poulton, S. J. Madden, B. Luther-Davies, and B. J. Eggleton, Cavity enhanced stimulated brillouin scattering in an optical chip for multi-order stokes generation, *Optics letters* **36**, 3687 (2011).
  - [12] E. A. Kittlaus, N. T. Otterstrom, and P. T. Rakich, On-chip inter-modal brillouin scattering, *Nature communications* **8**, 15819 (2017).
  - [13] O. Shlomovits, T. Langer, and M. Tur, The effect of source phase noise on stimulated brillouin amplification, *Journal of Lightwave Technology* **33**, 2639 (2015).
  - [14] P. Maker, R. Terhune, M. Nisenoff, and C. Savage, Effects of dispersion and focusing on the production of optical harmonics, *Physical review letters* **8**, 21 (1962).
  - [15] R. Behunin, P. Kharel, W. Renninger, H. Shin, F. Carter, E. Kittlaus, and P. Rakich, Long-lived guided phonons in fiber by manipulating two-level systems, *arXiv preprint arXiv:1501.04248* (2015).
  - [16] M. Nikles, L. Thevenaz, and P. A. Robert, Brillouin gain spectrum characterization in single-mode optical fibers, *Journal of Lightwave Technology* **15**, 1842 (1997).
  - [17] U. Fano, Effects of configuration interaction on intensities and phase shifts, *Physical review* **124**, 1866 (1961).
  - [18] M. F. Limonov, M. V. Rybin, A. N. Poddubny, and Y. S. Kivshar, Fano resonances in photonics, *Nature photonics* **11**, 543 (2017).
  - [19] M. F. Limonov, Fano resonance for applications, *Advances in optics and photonics* **13**, 703 (2021).
  - [20] M. Kroner, A. O. Govorov, S. Remi, B. Biedermann, S. Seidl, A. Badolato, P. M. Petroff, W. Zhang, R. Barbour, B. Gerardot, *et al.*, The nonlinear fano effect, *Nature* **451**, 311 (2008).
  - [21] R. W. Boyd, K. Rzaewski, and P. Narum, Noise initiation of stimulated brillouin scattering, *Physical review A* **42**, 5514 (1990).
  - [22] P. Kharel, R. O. Behunin, W. H. Renninger, and P. T. Rakich, Noise and dynamics in forward brillouin interactions, *Physical Review A* **93**, 063806 (2016).